Photocatalytic therapy via photoinduced redox imbalance in biological system

Kun Zhou[1,2,3,9], Lili Du[4,9], Rui Ding[5], Letian Xu[6], Shuai Shi[5], Siyuan Wang[2], Zaiyu Wang [3], Guoqing Zhang [7], Gang He [5] ✉, Zheng Zhao [1,2] ✉ & Ben Zhong Tang [1,2,3,8] ✉

Redox balance is essential for sustaining normal physiological metabolic activities of life. In this study, we present a photocatalytic system to perturb the balance of NADH/NAD$^+$ in oxygen-free conditions, achieving photocatalytic therapy to cure anaerobic bacterial infected periodontitis. Under light irradiation, the catalyst TBSMSPy$^+$ can bind bacterial DNA and initiate the generation of radical species through a multi-step electron transfer process. It catalyzes the conversion from NADH to NAD$^+$ (the turnover frequency up to 60.7 min^{-1}), inhibits ATP synthesis, disrupts the energy supply required for DNA replication, and successfully accomplishes photocatalytic sterilization in an oxygen-free environment. The catalyst participates in the redox reaction, interfering with the balance of NADH/NAD$^+$ contents under irradiation, so we termed this action as photoinduced redox imbalance. Additionally, animal experiments in male rats also validate that the TBSMSPy$^+$ could effectively catalyze the NADH oxidation, suppress metabolism and stimulate osteogenesis. Our research substantiates the concept of photoinduced redox imbalance and the application of photocatalytic therapy, further advocating the development of such catalyst based on photoinduced redox imbalance strategy for oxygen-free phototherapy.

There are hundreds of redox reactions in cells. Nutrients generate monomer and energy storage unit adenosine triphosphate (ATP) that can be taken in by cells through redox reactions to provide normal metabolic activities[1,2]. Redox balance thus plays a significant role in life activities[3]. Therefore, through the artificial intervention of the redox balance, the metabolic activity of the cells can be effectively regulated to achieve the effect of disease treatment. Actually, scientists have completed the treatment of cancer and microbial infections by human

intervention of redox balance[4–9]. Photodynamic therapy (PDT) is a typical example of breaking the redox balance in the cells through oxidative damage, thereby achieving therapeutic purposes[10–13]. The photosensitizer (PS) is a media that helps electron transfer or energy transfer to oxygen and biological substances to generate ROS under the participation of oxygen. Cell and biological substances were oxidized by the ROS, which leads to oxidation damage and redox imbalance[14–18]. Unfortunately, the oxygen-dependence characteristic

[1]Clinical Translational Research Center of Aggregation-Induced Emission, The Second Affiliated Hospital, School of Medicine, The Chinese University of Hong Kong, Shenzhen (CUHK-Shenzhen), Guangdong, China. [2]School of Science and Engineering, Shenzhen Institute of Aggregate Science and Technology, The Chinese University of Hong Kong, Shenzhen (CUHK-Shenzhen), Guangdong, China. [3]Hong Kong Branch of Chinese National Engineering Research Center for Tissue Restoration and Reconstruction, The Hong Kong University of Science and Technology, Kowloon, Hong Kong, China. [4]Department of Chemistry, The University of Hong Kong, Pokfulam, Hong Kong, China. [5]Frontier Institute of Science and Technology, Xi'an Jiaotong University, Xi'an, Shaanxi Province, China. [6]Guangdong Provincial Key Laboratory of Luminescence from Molecular Aggregates, South China University of Technology, Guangzhou, China. [7]University of Science and Technology of China, Hefei, Anhui, China. [8]AIE Institute, Guangzhou Development District, Huangpu, Guangdong, China. [9]These authors contributed equally: Kun Zhou, Lili Du. ✉e-mail: ganghe@mail.xjtu.edu.cn; zhaozheng@cuhk.edu.cn; tangbenz@cuhk.edu.cn

of PDT encounters challenges in treating anaerobic bacteria-infected diseases[19]. Besides, traditional antibiotics are prone to drug resistance and have a high recurrence rate[20,21]. Therefore, the treatment of anaerobic bacteria infection has always been a major scientific problem to be solved by researchers in the biomedical field. For example, periodontitis, often triggered by anaerobic bacteria, poses a significant challenge due to the complex microbial environment of the oral cavity. Antibiotics lack specificity for harmful bacteria and can disturb the balance of oral flora, potentially increasing the risk of recurrence[22]. To address these limitations, researchers have explored photothermal therapy (PTT) as an alternative treatment for periodontitis. PTT involves applying a photothermal agent to the affected area, which rapidly raises the local temperature, effectively killing the bacteria without harming surrounding healthy tissues[23,24]. Similarly, photodynamic therapy (PDT) has shown promising selectivity in targeting bacteria. However, its efficacy in treating anaerobic infections is hindered by the limited oxygen content, which is essential for the PDT process. If the redox balance in anaerobic bacteria can be disturbed through the redox catalysis in vivo, thereby inhibiting its normal metabolism, it would be a promising strategy to solve the problem that anaerobic bacteria-infected diseases are difficult to cure, and also to overcome challenge that traditional PDT doesn't work well in anaerobic condition.

NADH, as a coenzyme of dehydrogenase, is a key substance in cell physiological activities and participates in hundreds of biological redox reactions[25]. In the process of biological redox, NADH acts as a donor of protons and electrons, and NAD^+ acts as a receptor of protons and electrons. Electrons are transferred in the respiratory chain through the conversion of NADH to NAD^+ on the mitochondrial inner membrane, and ATP is synthesized to provide a guarantee for the normal operation of the electron transport chain (ETC) and energy metabolism in the cells (Fig. 1a)[23–25]. Therefore, by oxidizing NADH with a photocatalyst, the redox balance in anaerobic bacteria could be perturbed directly, thereby achieving photocatalytic therapy (PCT) in an anaerobic environment. Regarding the oxygen-independence property, PCT via photoinduced redox imbalance (PIRI) is a more advantageous phototherapy mode in particular for anaerobic infected diseases.

However, in order to realize oxygen-free PCT by redox imbalance in vivo, there is a stringent requirement for the catalyst used. First of all, the catalyst should be prone to generate electron transfer under photoactivation, while the construction of a D-A structure has been demonstrated to be an effective and simple strategy[26]. Until now, photooxidation catalysis of NADH to NAD^+ in a hypoxia environment has been realized by constructing intramolecular D-A structure[27,28], D-A supramolecular complex, and metal-coordinated D-A complex[29–31]. However, the time scale of the charge separation resulting from intramolecular electron transfer is too short[32,33], making it challenging to capture the intramolecular single electron transfer (SET) process of the catalyst, increasing the difficulty of exploring the underlying mechanism. Therefore, the researchers tried to solve the above problems through intermolecular electron transfer by constructing the D-A complex[34,35]. However, the composite system also has some defects, such as the intermolecular electron transfer is affected by the interaction distance[36,37], the introduced metal elements have biological safety risks[38], and extra biotarget carries the risk of missing the target[39]. Therefore, it is still a great challenge for scientists to construct a suitable charge transfer system to induce the redox imbalance and realize oxygen-free PCT in vivo.

Here, we constructed a potent photocatalytic system $TBSMSPy^+$, which showed highly catalytic activities through the photo-induced intramolecular multi-step electron transfer. The designed catalyst $TBSMSPy^+$ can effectively catalysis the oxidation of NADH, which disturbs the normal operation of the electron transport chain and inhibits ATP synthesis, blocking the energy supply of DNA replication, leading to cell death (Fig. 1b). We termed this action as photoinduced redox
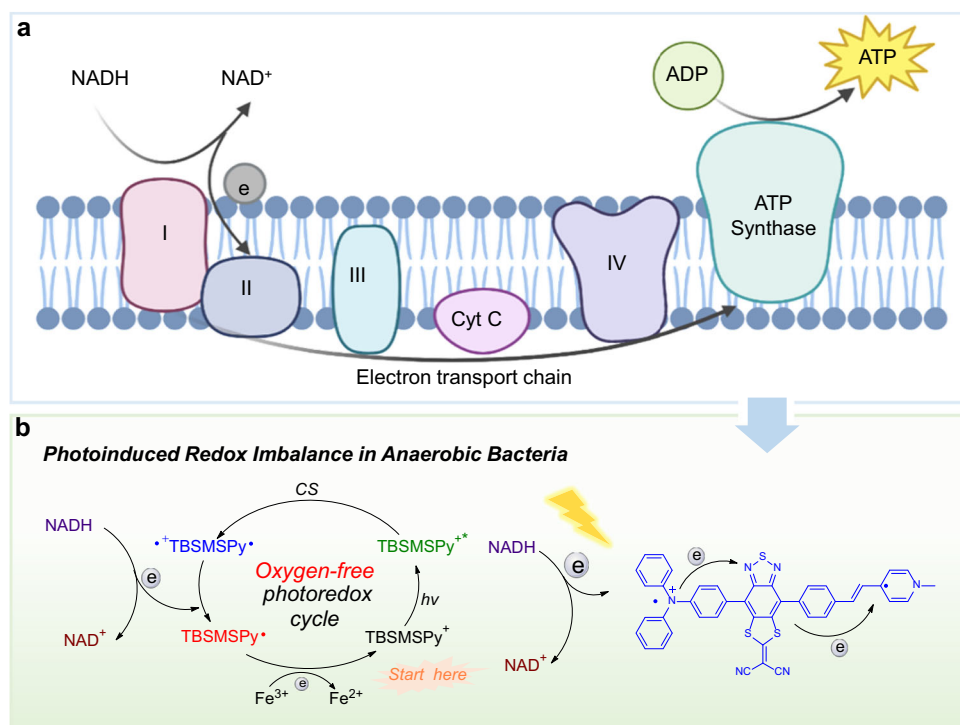

Fig. 1 | Photoredox catalysis in cells. a Schematic of the electron transport chain and metabolism-regulating the NADH/NAD^+ balance. Complex I: NADH-Q reductase; Complex II: $FADH_2$-Q reductase; Complex III: Cytochrome reductase; Complex IV: Cytochrome oxidase. Created in BioRender. Zhou, K. (2024) https://BioRender.com/q16n114. b Schematic illustration of photo-induced redox imbalance in anaerobic bacteria through multi-step electron transfer of $TBSMSPy^+$. CS: charge separation.
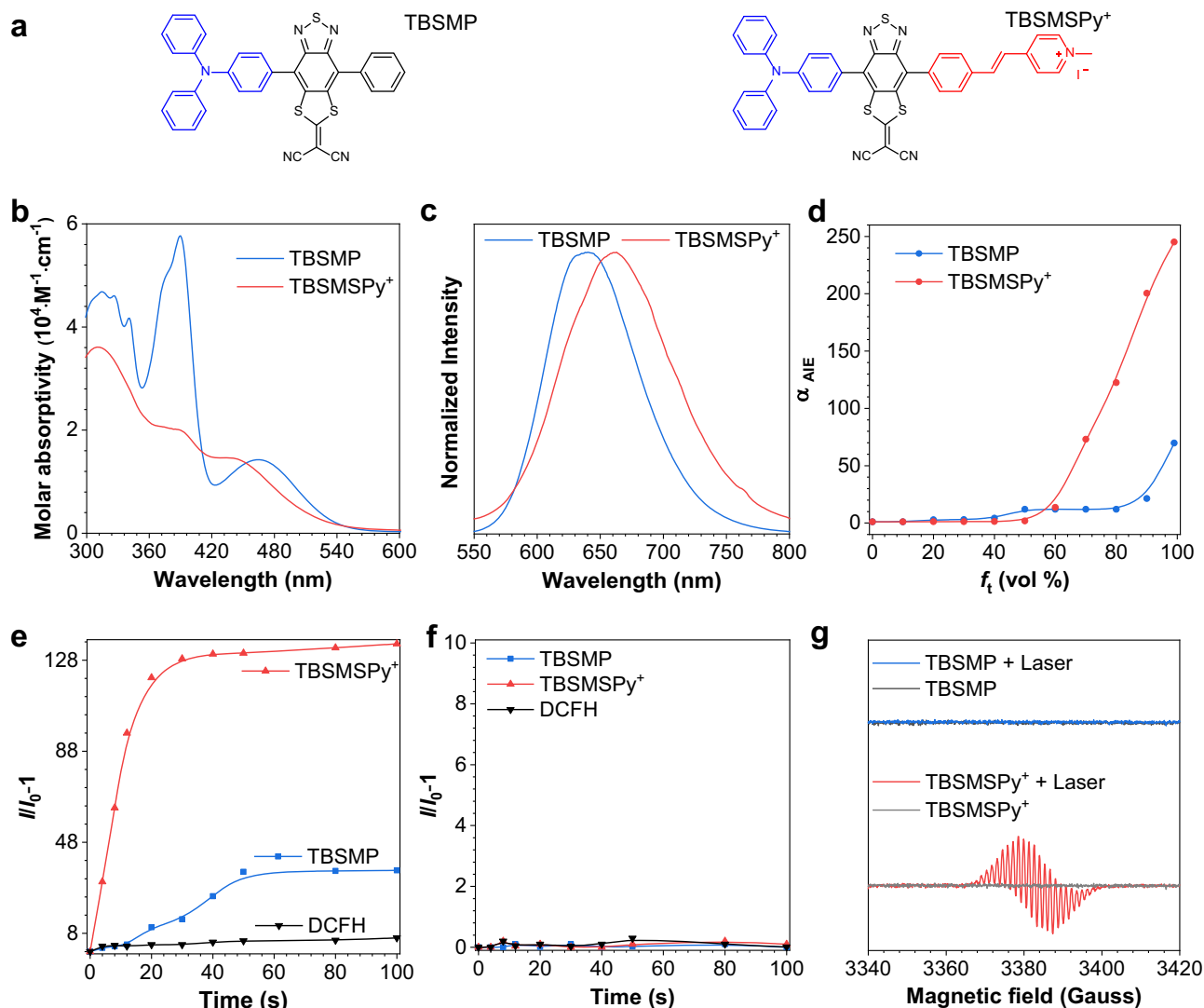
Fig. 2 | Optical properties. a Molecular structure of TBSMP, and TBSMSPy⁺. **b** UV-vis spectra of TBSMP and TBSMSPy⁺. **c** Normalized PL spectra of films of compounds. **d** The plots of the α_{AIE} versus the composition of the toluene mixture of TBSMP and TBSMSPy⁺ $\alpha_{AIE} = I/I_0$, $I_0 = $ PL intensity in pure DMSO. **e, f** Plots of relative PL intensity of DCFH (for general ROS detection) in the presence of TBSMP and TBSMSPy⁺ upon exposure to 450 nm laser (10 mW·cm⁻²) in air-saturated (**e**) and deoxygenated (**f**) solution. I_0 and I are the PL intensities of the indicator before and after irradiation, respectively. **g** Electron spin resonance (ESR) curves of TBSMP and TBSMSPy⁺ in DMF before and after exposure to 450 nm laser (10 mW·cm⁻²) in deoxygenated solution.

imbalance (PIRI) and demonstrated this strategy in periodontitis treatment. Compared with the reported catalyst system, our design 1) formed a highly reactive radical species through an intramolecular multi-step electron transfer strategy, which greatly improves the conversion efficiency from NADH to NAD⁺, resulting in a turnover frequency (TOF) of 60.7 min⁻¹. 2) PIRI brings a no-oxygen participation pathway for phototherapy in an anaerobic environment, which breaks the restriction of oxygen content to traditional PDT. 3) It can bind directly to bacterial DNA without extra biological targets, reducing the risk of missing targets in cells, and metal-free reducing toxicity to normal tissues.

Results

Molecular synthesis, property characterizations

All compounds, TBSMP and TBSMSPy⁺ were synthesized according to the synthetic route shown in Supplementary Fig. 1. All of the targeting compounds and intermediates have been fully characterized by ¹H NMR, ¹³C NMR, ¹⁹F NMR, and high-resolution mass spectra (Supplementary Figs. 21–42). The photophysical properties of the synthesized compounds have been investigated in solution. In general, the

absorption spectra of dimethyl sulfoxide (DMSO) solutions of the TBSMP showed three peaks at 316, 390, and 460 nm (Fig. 2b). TBSMSPy⁺ also has three absorption peaks at 311, 390, and 443 nm, respectively, in visible region, in which the former two originated from the local-excited (LE) states, while the latter one arose from the intramolecular charge transfer (ICT). The absorption of TBSMP and TBSMSPy⁺ in the range of 400 and 600 nm showed its strong visible absorption (Fig. 2b). Figure 2c is the normalized Photoluminescence (PL) spectra of two compounds in film. With increasing the D (donor)-A (acceptor) strength, the emissions of the two compounds showed a trend of TBSMP (639 nm) < TBSMSPy⁺ (662 nm) due to the gradually enhanced ICT (Fig. 2c). PL measurement showed that TBSMP and TBSMSPy⁺ had a stronger emission in film states, suggesting its aggregation-induced emission (AIE) characteristic. Thus, AIE features of two compounds were investigated in dimethyl sulfoxide (DMSO)/ toluene (TOL) mixtures via varying the fractions of toluene. As depicted in Fig. 2d and Supplementary Fig. 2a, b, the solution of TBSMP and TBSMSPy⁺ exhibited very weak emissions. With the toluene fraction in the mixed solvent increasing to 70%, the emission enhanced gradually. Afterward, along with continuously raising the fraction of toluene to

99%, the PL intensities of TBSMP and TBSMSPy$^+$ increased dramatically to their maximum, which was 70 and 245 times higher than those in pure DMSO solution, respectively, definitely indicating typical AIE characteristics. The lifetimes and absolute photoluminescence quantum yields (PLQYs) of two compounds were also measured. The absolute PLQYs of TBSMP and TBSMSPy$^+$ were 29.1% and 2.2%, respectively (Supplementary Table 1). Lifetime showed a similar trend to QY, 7.3 ns, and 2.5 ns, respectively (Supplementary Fig. 2c). The huge difference between the two compounds mainly came from the cationic pyridine moiety, leading to the weak QY value and lifetime of TBSMSPy$^+$ (Supplementary Fig. 2c and Supplementary Table 1). Notably, all of the compounds show significant solvatochromic effects (Supplementary Fig. 2d, e). For TBSMSPy$^+$, PL spectra are obviously affected by the polarity of solvents, and a redshift in its emission is observed. As shown in Supplementary Fig. 2d, the emission maximum of TBSMSPy$^+$ has a bathochromic shift from 551 nm to 656 nm with increasing solvent polarity. In addition, TBSMP showed the same trend, the emission has a redshift from 548 nm to 664 nm with the increased polarity of solvent (Supplementary Fig. 2e). These results indicated the strong D-A structure of TBSMSPy$^+$ promoted the ICT effects in a polar solvent, which is favorable for the electron transfer process in PCT.

Radical generation

The ROS generation ability was evaluated using various commercial fluorescence probes[40]. As depicted in Fig. 2e, all compounds exhibited substantial ROS generation under irradiation. As irradiation time increased, 2′,7′-dichlorofluorescin diacetate (DCFH) intensity showed a rapid rise within 60 s, particularly for TBSMSPy$^+$. It suggested that the introduction of cationic pyridine greatly enhances ROS generation. To identify the species of ROS, we initially assessed the singlet oxygen by 9,10-Anthracenediyl-bis(methylene)dimalonic acid (ABDA). In Supplementary Fig. 3a, TBSMP presented superior $^1O_2$ generation, which was better than Ce6, while TBSMSPy$^+$ showed negligible $^1O_2$ generation capability. We thus concluded that TBSMSPy$^+$ was more likely to be a type I PS. Further investigation indicated that TBSMSPy$^+$ could produce radical $O_2^{\cdot-}$ efficiently upon light irradiation, which was detected by dihydroethidium (DHE, Supplementary Fig. 3b). It is important to note that although type I PS could generate ROS in hypoxia conditions, it was not an oxygen-independent process[41]. Fig. 2f showed that both TBSMP and TBSMSPy$^+$ were inactive for ROS generation under deoxidation conditions upon irradiation, however, TBSMSPy$^+$ could generate radical signals upon photoirradiation relative to TBSMP (Fig. 2g). These results suggested that TBSMSPy$^+$ could work as a potential oxygen-free catalytic system to perturb the in vivo redox balance in either normoxia or hypoxia or even anaerobic environments through the generated radicals, thus enabling oxygen-independent photocatalytic therapy. It is worth noting that although type I PS can take effect in hypoxic conditions, its therapeutic potential in certain anaerobic environments remains restricted due to the lack of oxygen. Therefore, the oxygen-independent photocatalytic therapy approach may demonstrate an effective strategy to catalyze the oxidation of NADH and interfere with the in vivo redox balance, thus achieving the therapeutic effect under normoxia or anaerobic environments.

To further understand the radical generation mechanism, the EPR was employed to explore the radical species of TBSMSPy$^+$ under different atmospheres. As shown in Supplementary Fig. 3c, TBSMSPy$^+$ showed weak EPR signals without any trapping agent in an air-saturated solution upon irradiation, displaying no hyperfine splitting. The EPR signals are identical to the reported ones for radicals of triphenylamine (TPA) derivatives, which suggested that the radical signals of TBSMSPy$^+$ under normal conditions may originate from TPA$^{\cdot+}$[42]. Furthermore, several works have reported cationic pyridine had low redox potential, which easily accepted electrons in the Ar atmosphere, resulting in the formation of neutral pyridine radicals (Py$^\cdot$) under

irradiation[43]. Therefore, the strong EPR signals of TBSMSPy$^+$ with hyperfine splitting under the Ar atmosphere were assigned to the electron transfer from TPA$^{\cdot+}$ to the cationic pyridine, resulting in the formation of pyridine radical species[44]. Based on the abovementioned experimental data, the radical generation mechanism of TBSMSPy$^+$ in anaerobic conditions could be elucidated as follows: TPA moiety loses electrons to form TPA$^{\cdot+}$ upon excitation, followed by the acceptance of an electron by cationic pyridine, resulting in the formation of Py$^\cdot$, which may either be kept in inert gas sphere or captured by atmospheric oxygen to form $O_2^{\cdot-}$, which then proceeded to the Type I process. This electron transfer behavior generated active radical species $^{\cdot+}$TBSMSPy$^\cdot$ would facilitate the catalysis of NADH oxidation, initiating the designed cellular PIRI process. A comparison of the ROS generation and EPR results clearly indicated that the designed catalyst is no longer constrained by the oxygen content, it could switch the pathway in different atmosphere. Under aerobic conditions, it tended towards the type I pathway, while in anaerobic conditions, the intrinsic radicals of the catalyst could execute the PIRI pathway, facilitating the oxidation of NADH and going to the photocatalytic therapy model. This conversion perfectly addressed the limitation of traditional PDT on oxygen dependence.

Photoinduced electron transfer mechanism study

To gain a more profound understanding of the underlying mechanism for the generation of the intrinsic radical species through the photocatalysis process, femtosecond transient absorption (fs-TA) was employed. It has proved to be a powerful technique in studying the inter and intramolecular electron transfer process[45–47]. We employed fs-TA to study the electron transfer processes of TBSMSPy$^+$ and the control molecules after irradiation in THF solvent. As shown in Fig. 3a, after excitation by a 400 nm pulse pump, PBSMP showed a negative signal at 460 nm, which was attributed to the stimulated emission (SE) band. In addition, the excited state band (ESA) at 660 nm is mainly assigned to the absorption of the singlet excited states of PBSMP from the S_1 to S_n, which decays in the next 6 ns (Fig. 3b, c and Supplementary Fig. 4a). The fs-TA spectra of TBSMP were displayed in Fig. 3d–f and Supplementary Fig. 4b, c. As shown in Fig. 3d, unlike the spectra obtained for PBSMP, an intense absorption band at 520 nm showed up initially, which indicates that the TPA moiety of TBSMP was mainly excited. Obviously, the BSM moiety of TBSMP might be partially irradiated due to the absorption band obtained at 660 nm. Later (Fig. 3e), the observed growth of the SE band at 750 nm from 1.65 ps to 66.1 ps could be due to the formation of the emissive charge-separated species through an electron transfer process from the TPA moiety to the BSM moiety. The dramatic red-shifting from 460 nm to 750 nm fully explained the much lower energetic level of the charge-separated species compared to the S_1 of PBSMP.

Surprisingly, unlike the photoinduced electron transfer observed for TBSMP, the fs-TA results obtained for the PBSMSPy$^+$ tell a different story after introducing the cation Pyridine (Py) into the BSM structure. As shown in Supplementary Fig. 5, the EAS band of BSM at 650 nm was first observed, which decayed in the next 12 ps following with a new EAS band appearing at 470 nm. The apparent isosbestic point at 520 nm indicated the conversion between two distinct states, which could be assigned to the electron transfer process from BSM* to cationic pyridine, and a new non-luminescent charge-separated species was generated (PBSMSPy$^\cdot$).

Encouraged by the photoinduced electron transfer process from TPA to BSM and BSM to Py, respectively, it was speculated that the introduction of TPA, BSM, and Pyridine into the one molecular skeleton would produce a multi-step intramolecular electron transfer process. Thus, the fs-TA of TBSMSPy$^+$ was also analyzed. As shown in Fig. 3g, two obvious EAS bands at 530 and 670 nm were obtained. Compared with previous results, the absorption band at 670 nm belonged to the EAS band of the BSM. With the decreased intensity of
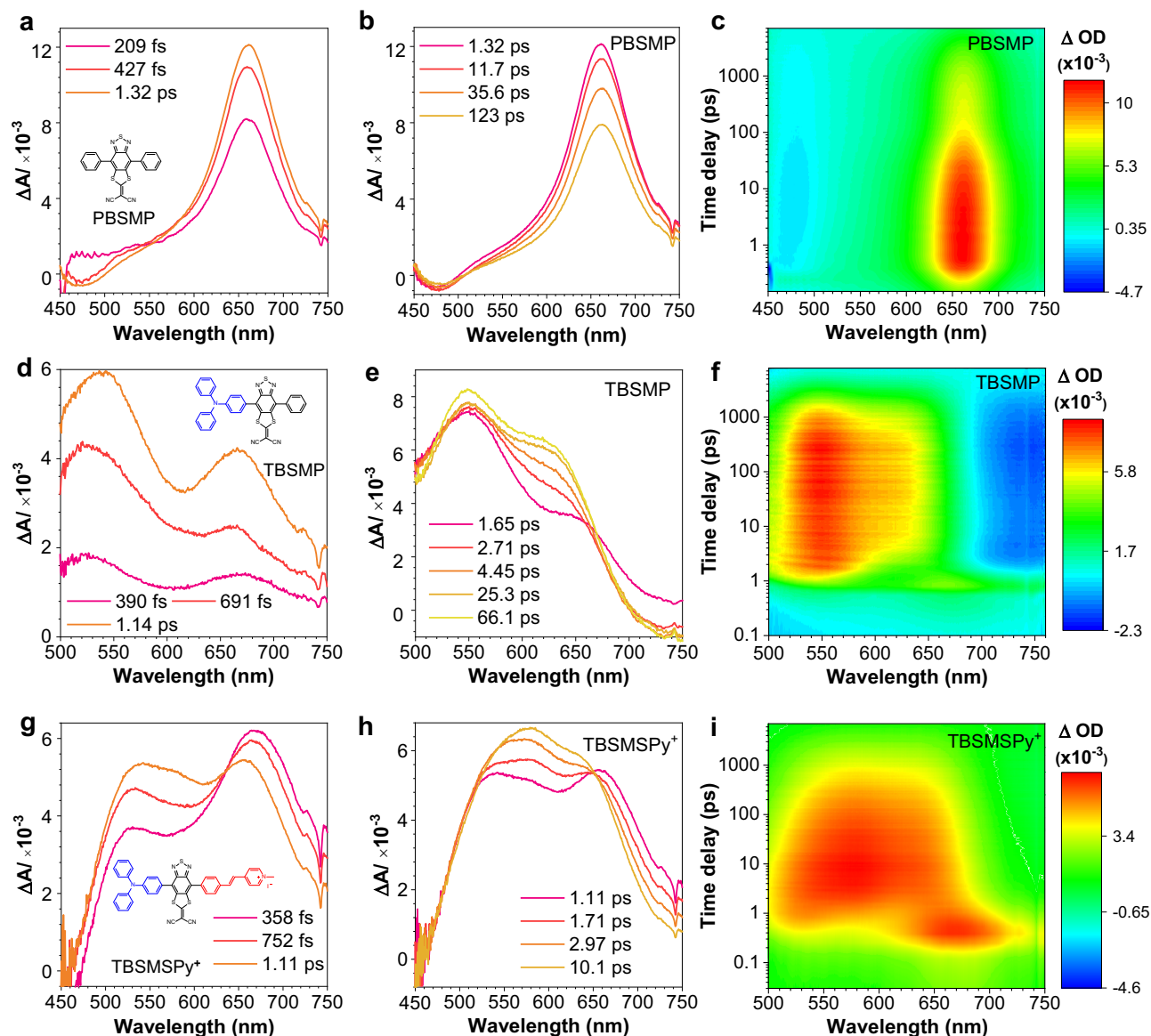
Fig. 3 | Ultrafast time-resolved spectroscopy. The fs-TA spectra of PBSMP (**a**, **b**), TBSMP (**d**, **e**), and TBSMSPy+ (**g**, **h**) were obtained at different time delays acquired after 400 nm excitation. Three-dimensional femtosecond transient absorption spectra of PBSMP (**c**), TBSMP (**f**), and TBSMSPy+ (**i**).

670 nm, the absorption band at 530 nm gradually increased. Later, with the subtle gradation of the EAS band at 670 nm, a broad EAS band at 550 nm showed up in Fig. 3h and Supplementary Fig. 4d. Three-time constants of 1.1 ps, 131.8 ps and 2.4 ns were obtained by fitting the kinetics at 573 nm (Supplementary Fig. 6d), and obvious separated HOMO and LUMO (Supplementary Fig. 7) implied the potential multi-step involved intramolecular electron transfer process[48–50]. This multi-step intramolecular electron transfer behavior stabilized the radical species generated by TBSMSPy+ and promoted the PIRI process. Moreover, the CV curve also indicated the redox properties of TBSMSPy+, which may regulate redox balance in the biosystem (Supplementary Fig. 8).

Photoinduced perturbation of NADH/NAD+ balance

Since NADH participates in the maintenance of the intracellular redox balance in many oxidoreductases as an important coenzyme, the oxidization of NADH in cells would disturb the intracellular redox balance, thus leading to cell death[51]. Motivated by the radical generation ability of the designed catalyst via multi-step electron transfer upon irradiation, we postulated that the multi-step electron transfer of TBSMSPy+

promoted the radical species generation, which would catalyze the oxidation of NADH. Consequently, a detailed catalytic mechanism was proposed. As shown in Fig. 4a, TBSMSPy+ initially was excited under light irradiation and formed the triplet excited state TBSMSPy+*. Subsequently, the photo-induced electron transfer happened with charge-separated species •+TBSMSPy• production. Later, the strong oxidized TPA•+ moiety could rap the electron from NADH and catalysis the conversion of NADH to NAD+, interfering with the balance of NADH/NAD+ content and leading to bacteria death. As a photocatalysis agent, an intermediate form of catalyst needs to be converted back to its initial active form to complete the catalytic cycle. Therefore, under anaerobic conditions, TBSMSPy• further gave the electron to Fe^{3+} (methemoglobin, nutrition of *P. gingivalis*) to obtain Fe^{2+} and returned to the original state TBSMSPy+. Conversely, under aerobic conditions, the O_2 would obtain electrons from TBSMSPy• and generate $O_2^{-•}$ (Type I).

To demonstrate our proposal, the ability of two molecules to catalyze the oxidation of NADH was investigated. As shown in Fig. 4b, c, under anaerobic conditions, when added hemin (Fe^{3+}), the absorption of NADH at 339 nm decreased both in TBSMP and
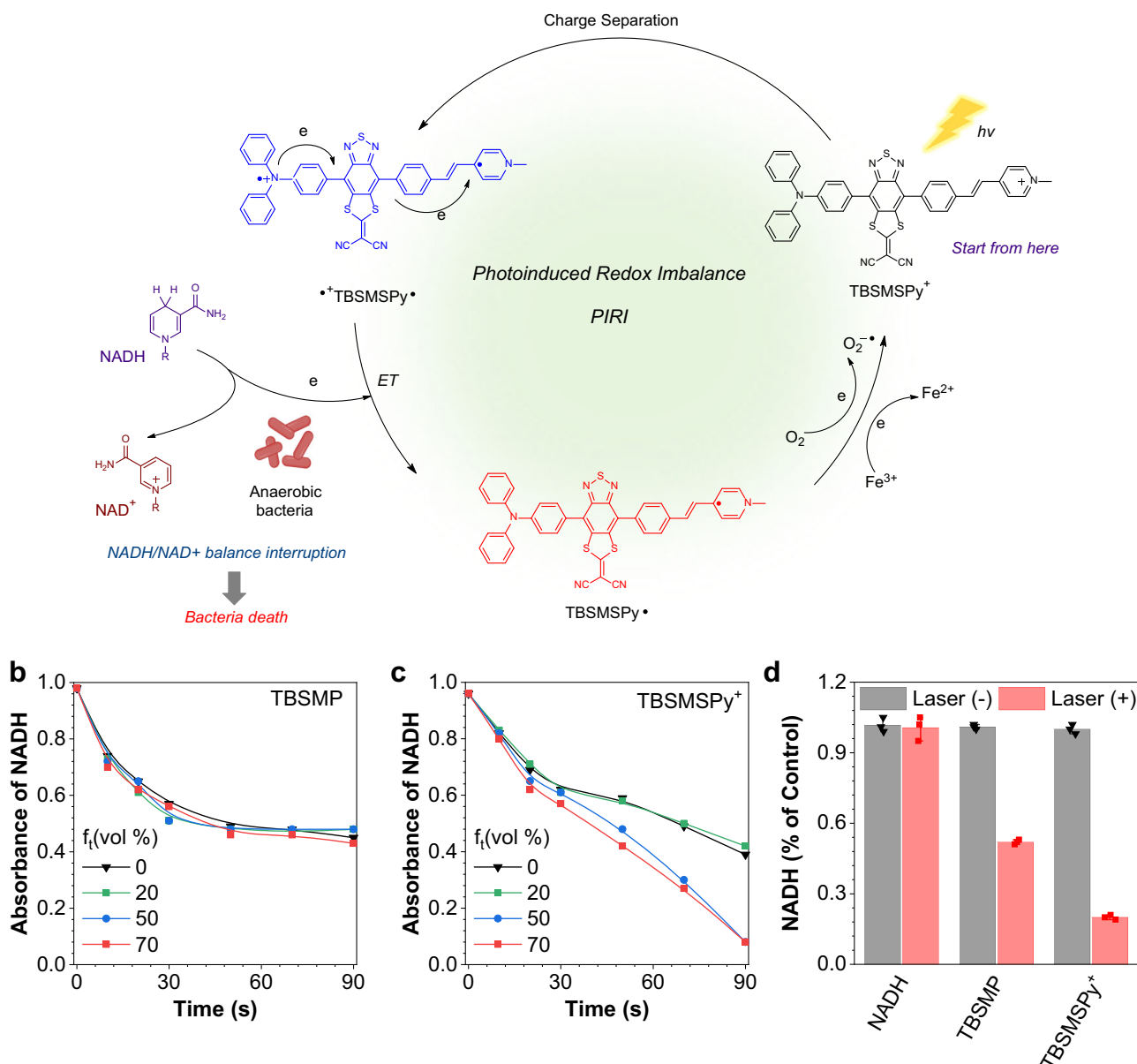
a   *Photo-induced redox imbalance (PIRI)*

Fig. 4 | Photo-induced redox imbalance mechanism. a The Schematic showing the proposed photo-induced redox imbalance in anaerobic bacteria. The anaerobic bacteria cartoon was created in BioRender. Zhou, K. (2024) https://BioRender.com/b96y986. **b, c** Absorbance changes of NADH (180 µM) at 339 nm after photocatalytic oxidation by 3 µM TBSMP (**b**) and TBSMSPy$^+$ (**c**) with Fe^{3+} in deoxygenated TBSMSPy$^+$ solution. **d** Quantitative analysis of NADH level in bacterial suspension treated with TBSMP and TBSMSPy$^+$ at laser irradiation and without irradiation. Data are presented as mean ± s.d. derived from $n = 3$ independent biological samples. *ET*: electron transfer; e: electron.

TBSMSPy$^+$ solution. To ensure the success of the catalysis, NMR measurement was carried out to identify the production. In Supplementary Fig. 10, the newly formed peaks of NAD$^+$ were observed at 8.01, 8.28, 8.97, 9.33, and 9.64 ppm in the presence of TBSMSPy$^+$, confirming the photo-oxidative reaction from NADH to NAD$^+$ under light irradiation. And no NAD$^+$ signal was detected in the unirradiated TBSMSPy$^+$ solution. Besides, stable NADH absorption was also observed under irradiation (Supplementary Fig. 9e), indicating TBSMSPy$^+$ acted as a photocatalyst in NADH/NAD$^+$ conversion. The TOF of TBSMSPy$^+$ for NADH oxidation was calculated to be 60.7 min^{-1} (Fig. 4c), which is much higher than that of previously reported photocatalysts (Supplementary Table 3). Furthermore, TBSMSPy$^+$ demonstrated excellent efficiency under mild catalytic conditions such as soft light power,

short irradiation time, and oxygen independence, highlighting its potential in photocatalytic therapy (Supplementary Table 3). Compared to TBSMP (TOF is 37.9 min$^-$), the cationic moieties of TBSMSPy$^+$ facilitated intermolecular interaction and promoted electron transfer in aggregation, thus enhancing catalytic efficiency. While, in the absence of Fe^{3+}, the absorption of NADH showed a slight decrease within the former 30 s and then kept at a stable level (Supplementary Fig. 9a). Thus, in a deoxygenated environment, Fe^{3+} acted as an electron acceptor to help TBSMSPy$^+$ go back to the original state rapidly and continue the catalysis. Moreover, under aerobic conditions, we conducted an evaluation of the oxidative ability of two compounds. In line with our expectations, the O$_2$ also plays a similar role as that of Fe^{3+}. In Supplementary Fig. 9b–d, the absorption of NADH also showed

a declining pattern, concomitant with the $O_2^{-\bullet}$ generation. Considering the TBSMSPy$^+$ showed good catalytic performance in aggregation, the Gibbs-free energy of the photoinduced electron transfer between TBSMSPy$^+$ was calculated using the Rehm Weller equation (Supplementary Fig. 44)[52]. Rehm−Weller theory calculations show that the ΔG is − 124.6 kJ/mol, which indicates photoinduced intermolecular electron transfer of TBSMSPy$^+$ between excited-state and ground-state is thermodynamically feasible. Therefore, the intermolecular electron transfer contributes to photoinduced redox imbalance (PIRI). Upon irradiation, TBSMSPy$^+$ goes to the excited state (TBSMSPy$^{+\ast}$). Subsequently, electron transfer occurs between the TBSMSPy$^{+\ast}$ and nearby ground-state TBSMSPy$^+$ to generate free radical ion pairs, TBSMSPy$^{+\bullet}$ and TBSMSPy$^\bullet$. TBSMSPy$^{+\bullet}$ returns to a cationic state by oxidizing NADH. The TBSMSPy$^\bullet$ further transfers an electron to Fe^{3+} or oxygen to produce Fe^{2+} or $O_2^{-\bullet}$, respectively, in different atmospheres (Supplementary Fig. 44d). Then we utilized anaerobic bacteria to evaluate the catalytic ability of two molecules in an anaerobic environment. As shown in Fig. 4d, ~ 80% of NADH was oxidized when TBSMSPy$^+$ was added to the anaerobic bacterial suspension after irradiation. TBSMP also showed a 48% reduction in NADH. These results reflected the superior oxidation ability of TBSMSPy$^+$. TBSMSPy$^+$ exhibited higher activity than TBSMP due to the pronounced electron-withdrawing properties of the pyridine moiety in TBSMSPy$^+$. This observation aligns with the findings from fs-TA spectra that the electrophilic cationic pyridine group endowed the TBSMSPy$^+$ multi-step intramolecular electron transfer behavior, which stabilizes the radical species generated by TBSMSPy$^+$ and benefitted PCT (Fig. 3). Particularly, this photocatalysis was an oxygen-independent process, which represented a significant milestone in the field of phototherapy.

In vitro photocatalytic antibacterial therapy and mechanism study

Inspired by the impressive PIRI effects of two catalysts, the phototoxic of TBSMP and TBSMSPy$^+$ were investigated. Two typical anaerobic periodontal pathogens, *P. gingivalis* and *F. nucleatum* were chosen to evaluate antibacterial activity under irradiation. In addition, commercial minocycline hydrochloride ointment (PERIO) as an antibiotic against periodontal pathogens was selected as the positive control. As illustrated Fig. 5a, b, and Supplementary Fig. 11, several bacterial colonies survived in irradiated TBSMSPy$^+$ plant, demonstrating a 99.2% bacterial killing ratio against *P. gingivalis*, surpassing the efficacy of the positive control (Supplementary Fig. 11). Irradiated TBSMP also showed 63.2% killing ratio indicated the significant involvement of the TPA moiety in PIRI process, resulting in a high photocatalytic biocidal effect. Similarly, *F. nucleatum* showed a similar trend in bacterial killing results. In Fig. 5a, b, TBSMSPy$^+$ presents a 99.7% killing ratio against *F. nucleatum*, and the race colony-forming units (CFU) were also observed on the PERIO plant. A relatively mild phototoxicity was also presented by irradiated TBSMP (24.3%). In addition, other oral flora were also employed to evaluate the antibacterial activity of TBSMSPy$^+$. As shown in Supplementary Table 2, TBSMPy$^+$ exhibited superior antibacterial activity against *E. faecalis, S. aureus, and S. mutans*, with a high killing rate of over 85%, which indicates the TBSMPy$^+$ has potential for oral sterilization therapy.

Encouraged by the excellent antibacterial activity of TBSMSPy$^+$ through the PIRI pathway, the antibacterial mechanism has become an attractive exploration. Thus, the Confocal Laser Scanning Microscopy (CLSM) was employed to observe the interaction between molecules and bacteria[53]. As illustrated in Fig. 5c, d, TBSMSPy$^+$ could aggregate in the internal bacteria after a short time of incubation. Notably, the filamentous green emission of TBSMSPy$^+$ was observed in *P. gingivalis* which was similar to the nucleoid of bacteria. For *F. nucleatutm*, there was also a long stripe of green fluorescence emitted from the internal of bacteria. These results reflected that TBSMSPy$^+$ may have the potential to bind DNA. To confirm this hypothesis, the commercial

nuclear staining dye DAPI was applied to co-staining bacteria with TBSMSPy$^+$. The merged images and high colocalization coefficient (0.943 for *P. gingivalis*, 0.831 for *F. nucleatutm*) indicated that TBSMSPy$^+$ could accumulate and bind the DNA of bacteria. In addition, a slight green emission was also observed on the surface of bacteria due to the electrostatic interaction between the negative charge of the membrane of bacteria and the positive charge of TBSMSPy$^+$[54]. To confirm the binding interaction between the TBSMSPy$^+$ and DNA, The isothermal titration calorimetry (ITC) experiment was conducted. As illustrated in Supplementary Fig. 11, with the addition of the DNA into the TBSMSPy$^+$, the initial ΔH was around − 12 kcal/mol. It indicated that the initial interaction between DNA and TBSMSPy$^+$ was an exothermic process. In this process, the equilibrium association constant (K) for the interaction between the DNA and TBSMSPy$^+$ is $1.4 \times 10^5 M^{-1}$, indicating an obvious interaction between them, which helps to form the TBSMSPy$^+$-DNA complex. In addition, the DLS was employed to measure the particle size of the TBSMSPy$^+$ and DNA mixture solution. As illustrated in Supplementary Fig. 12a, b, the DNA size increased from 4.187 nm to 4.740 nm after mixing with TBSMSPy$^+$, this result revealed that the TBSMSPy$^+$-DNA complex was formed, which was consistent with CLSM images. The formation of the TBSMSPy$^+$-DNA complex led to the presence of TBSMSPy$^+$ within bacterial cells in an aggregate state, likely enhancing PIRI and improving antibacterial activities. To demonstrate this conjecture, the catalytic ability of the TBSMSPy$^+$-DNA complex was evaluated compared with a single molecule. Supplementary Fig. 12c presented that the TBSMSPy$^+$-DNA complex showed an excellent catalytic effect in NADH/NAD$^+$ conversion, which was equivalent to the aggregation results of TBSMSPy$^+$ (Fig. 4c). Nevertheless, the reason for the better performance of the TBSMSPy$^+$-DNA complex compared to the individual molecule remained to be elucidated. In pursuit of an answer to this question, we explored the phosphorescent lifetime of the TBSMSPy$^+$-DNA complex. In Supplementary Fig. 12d, the phosphorescent lifetime of the TBSMSPy$^+$-DNA complex was 3.52 ms, which was six-fold longer than a single molecule (0.57 ms). The long-lived triplet state of the TBSMSPy$^+$-DNA complex contributed to the stability of the charge separation state ($^{+\bullet}$TBSMSPy$^\bullet$) and promoted radical generation, facilitating electron transfer from the catalyst to NADH, consequently enhancing the efficiency of PIRI.

After clarifying that the TBSMSPy$^+$ bound to bacterial DNA and interfered with the redox balance in bacteria, the effects of TBSMSPy$^+$ on bacterial DNA were investigated. In general, the balance of NADH/NAD$^+$ directly influenced the ATP synthesis[55]. Hence, we proposed that the antibacterial mechanism of the TBSMSPy$^+$ might originate from the perturbation of the oxidation process of NADH in bacteria, which limited the synthesis of ATP and thus affected the replication process of DNA. Subsequently, we examined the impact of TBSMSPy$^+$ on DNA using a comet assay. Initially, an ATP inhibitor was added to the bacteria solution to limit the DNA replication process as a positive control. Figure 5e showed that there were almost no stain tails observed for bacteria incubated with unirradiated TBSMSPy$^+$ groups and negative control (only bacteria without any treatment), implying negligible DNA damage resulting from these treatments and also elucidating the limited antibacterial activity of these groups. In marked contrast, for both the positive group and bacteria incubated with irradiated TBSMSPy$^+$, stain tails were clearly presented, indicating effective damage to DNA. Typically, the high degree of DNA fragmentation indicated strand breaks of nucleoids in bacteria. Compared with positive groups, the irradiated TBSMSPy$^+$ group exhibited the same trend on the statistical tail length, olive tail moment and tail moment (Supplementary Fig. 13a–c). This phenomenon is primarily attributed to the lack of energy supply (due to the inadequate ATP supplement), resulting in blocked DNA replication and the formation of numerous fragments. As is well-known, DNA replication requires a large amount of energy supply[56–58]. ATP production, serving as the cellular energy reservoir, is crucial for sustaining cell viability[59,60]. The conversion of NADH to

NAD^{+} is concomitant with the substantial generation of ATP[2]. Nevertheless, an imbalanced NADH/NAD^{+} ratio would result in inadequate ATP levels, consequently affecting DNA replication[61], and thus leading to the huge fragmented DNA in the irradiated TBSMSPy[+] group (Fig. 5e). Furthermore, the ATP level in bacteria was also evaluated to prove this comment. As shown in Supplementary Fig. 13d, after
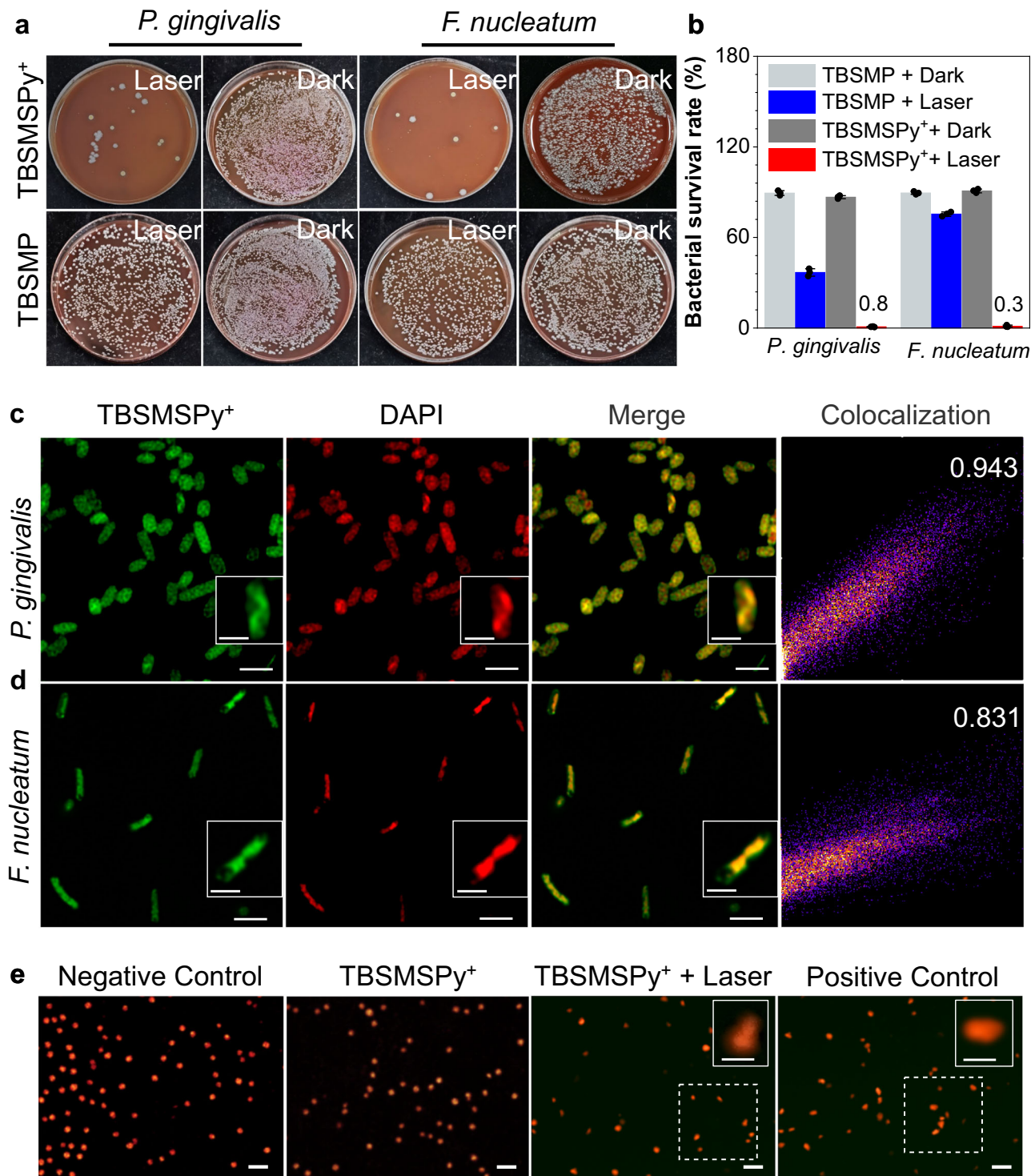

Fig. 5 | Photodynamic antibacterial activities in vitro. a Photograph of a BHI agar plate containing 5% sheep blood and biocidal activity of *P. gingivalis* and *F. nucleatum* with TBSMP and TBSMSPy[+] treatment under irradiation and without irradiation. **b** The bacterial survival rate of different treatment groups. Data are presented as mean ± s.d. derived from *n* = 3 independent biological samples. **c, d** CLSM images and colocalization analysis of *P. gingivalis* (**c**) and *F. nucleatum* (**d**) stained with TBSMSPy[+] (green), DAPI (red), respectively (*n* = 3 biologically independent samples, all views show similar results). TBSMSPy[+] channel: λex: 500 nm, λem: 600–750 nm; DAPI channel: λex: 405 nm, λem: 425–490 nm. Scale bars, 3 μm, inserted images Scale bars, 1 μm. **e** Comet assays for direct observation of DNA damages of bacteria subjected to the following different treatments (*n* = 3 biologically independent samples, all views show similar results). Negative Control: only bacteria; Positive Control: bacteria treated with ATP inhibitor Calcimycin. Scale bars, 250 μm, inserted images Scale bars, 100 μm. Propidium iodide channel: λex: 540 nm, λem: 560–620 nm.

treatment with TBSMSPy$^+$, bacteria cells under irradiation dramatically lost their ability to produce ATP, implying that the TBSMSPy$^+$-mediated PIRI was active and blocked ATP supplement of DNA replication. Based on the aforementioned findings, a potential antibacterial mechanism was proposed as follows: (i) TBSMSPy$^+$ aggregated within bacteria cells and accumulated on DNA. (ii) Concurrently, the TBSMSPy$^+$ generated radical species perturbed the NADH/NAD$^+$ conversion, impeding ATP synthesis. (iii) This interference resulted in the cessation of DNA replication, leading to extensive DNA damage and a profound biocidal effect.

After elucidating the antibacterial mechanism of the PIRI pathway, we hoped to further prove it in animal experiments. Therefore, the relative antibacterial factors, *e.g.*, concentration, irradiation time, and irradiation power, were measured to optimize the condition for periodontitis therapy. As shown in Supplementary Fig. 14, the bacterial killing rate gradually rose with the concertation of TBSMSPy$^+$ increase from 0.25 to 2 μM, with optimal efficiency at 1 μM against *P. gingivalis* and 0.6 μM against *F. nucleatum*. At a concentration of 1 μM, the bacterial killing rate grew with laser power, arriving at its maximum at 50 mW/cm^2. Irradiation time is also an important aspect of our consideration. With 3 min irradiation, TBSMSPy$^+$ exhibited the best behavior against *P. gingivalis* and *F. nucleatum* (Supplementary Fig. 14c, f). Hence, 1 μM, 50 mW/cm^2 laser density, and 3 min irradiation time of TBSMSPy$^+$ were selected as optimal parameters for in vivo study.

Periodontitis treatment

Inspired by the effective photocatalytic antibacterial activity of TBSMSPy$^+$ in vitro, the PCT in vivo was investigated by using a periodontitis rats model (Fig. 6a). The detailed model establishment is described in Supplementary information (experimental part). To ensure the TBSMSPy$^+$ could stay in periodontal pockets for PCT during irradiation, the temperature-sensitive injectable hydrogels were employed as a substrate to load TBSMSPy$^+$. After fabrication, TBSMSPy$^+$ kept the AIE property in hydrogels. The orange emission was observed by naked eyes under UV light (Fig. 6b). In addition, it could keep a gel state at 37 °C, which makes the TBSMSPy$^+$ stay in the infected periodontal pockets for a long time and promotes therapeutic efficiency. Before the in vivo study, the biosafety of TBSMSPy$^+$ loaded hydrogel was investigated. As shown in Supplementary Fig. 15a, clear cell morphology and macroscopical proliferation were observed in the irradiated TBSMSPy$^+$ group, which were no differences from the control group. Moreover, the cell viability showed the irradiated TBSMSPy$^+$ group exhibited great proliferation from 100% to 290% for 3 days of incubation, which was similar to the control group. These results indicated the TBSMSPy$^+$ loaded hydrogels were friendly to oral cells and promoted cell proliferation. Thus, it is suitable to touch with oral epithelial tissue for periodontitis treatment (Supplementary Fig. 15b). The biodegradation results of TBSMSPy$^+$ Gel indicated the gel could degrade in saliva atmosphere after 2 days incubation (Supplementary Fig. 16a), which was biocompatible and suitable to be used as an oral ointment. By doing the above preparation, the in vivo treatment was scheduled. As shown in Fig. 6c, the maxillary second molar was fixed with orthodontic steel during the periodontitis modeling. The periodontitis was treated by injectable TBSMSPy$^+$ gel, followed by illumination of a 450 nm laser (0.05 W/cm^2) for 3 min, and the periodontitis would experience the process of inflammation and tissue repair. As the periodontitis lesion was close to superficial tissue and the 450 nm light source had weak tissue penetration ability, which prevented the deep tissue damage, the treatment under 450 nm light irradiation was appropriate for superficial periodontitis[62]. Moreover, the commercial medicine PERIO was injected into the periodontal pocket for periodontitis treatment as a positive control. The active ingredient of PERIO is 2% minocycline hydrochloride, which has been proven to be effective in the treatment of periodontitis and has been widely used in clinical treatment[63–65].

The 3D reconstructions of the maxillary molar area by micro-CT in the five groups (Infection, Healthy, PERIO, TBSMSPy$^+$ + Gel + Laser, TBSMSPy$^+$ + Gel, Gel + Laser,) after 21 days of treatment were conducted (Fig. 6d and Supplementary Fig. 17a). The corresponding degree of alveolar bone loss was quantitatively evaluated by the red lines, marking the distance between the cementoenamel junction (CEJ) and the alveolar bone crest (ABC)[66]. Evidently, the irradiated TBSMSPy$^+$ Gel group (0.55 mm) had a smaller CEJ-ABC distance than the unirradiated TBSMSPy$^+$ Gel group (1.16 mm) and positive PERIO-treated group (1.05 mm). It was also observed that there was no significant difference in CEJ-ABC distance between the healthy group (0.53 mm) and irradiated TBSMSPy$^+$ Gel group (Fig. 6f and Supplementary Fig. 17c). Moreover, the irradiated TBSMSPy$^+$ Gel group also presented the best outcome of improved trabecular features, such as bone volume per tissue volume (BV/TV × 100%) (Fig. 6g and Supplementary Fig. 17d). Compared with the healthy group (BV/TV% = 40.5%), the BV/TV values in infected group were significantly reduced to 26.3%, which indicated apparent alveolar bone loss and confirmed the successful establishment of the chronic periodontitis model. The BV/TV value in the irradiated TBSMSPy$^+$ Gel group (39.7%) was close to the healthy group level (40.5%), while for the pristine hydrogel group and unirradiated TBSMSPy$^+$ Gel group, the corresponding values were 27.6% and 29.3%, demonstrating the efficacy treatment and the self-repairing compacity closely correlated with the photoactivable TBSMSPy$^+$. However, when the hydrogel was loaded with PERIO, the BV/TV (28.7%) exhibited a similar value as the infection group, which suggested that PERIO treatment is not as effective as photocatalytic therapy in preventing alveolar bone loss. The results unequivocally confirmed that the therapeutic effect of irradiated TBSMSPy$^+$ Gel was significantly better than the clinical antibiotic agent (PERIO). Besides, the Tb.N and Tb. Th in the irradiated TBSMSPy$^+$ group were 3.3/mm and 0.15 mm respectively, indicating the excellent performance of light-irradiated TBSMSPy$^+$ against alveolar bone loss (Supplementary Fig. 45). However, unirradiated TBSMSPy$^+$ and blank gels present no difference between infected group (Tb. N is 1.17/mm, Tb. Th, 0.1 mm). Moreover, the low value of trabecular separation in irradiated TBSMSPy$^+$ also indicated great potential for inhibiting alveolar bone loss in treating periodontitis (Supplementary Fig. 45c).

To further evaluate the therapeutic effects of TBSMSPy$^+$ Gel, a histological analysis was conducted to investigate the inflammatory responses and periodontium status. In Fig. 6e and Supplementary Fig. 17b, the H&E staining results showed a large area inflammatory response and tanglesome periodontium in infection, unirradiated TBSMSPy$^+$ Gel, and irradiated Gel groups. Whereas the PERIO-treated group showed a more significant anti-inflammatory response than the above control groups. The irradiated TBSMSPy$^+$ group presented minimum inflammatory reaction, revealing the effective photocatalytic antibacterial activity in vivo of TBSMSPy$^+$ Gel. The great biocidal effects in vivo confirmed again that the PIRI strategy has worked in living systems successfully.

Moreover, the expression level of osteogenesis cytokines is also an important index to assess the therapeutic effects[67]. In Supplementary Fig. 18a–c, the expression levels of Runx2, OCN, and ALP in the control group (unirradiated TBSMSPy$^+$ Gel, irradiated Gel, infection) were much lower than those in the healthy group, demonstrating the successful establishment of the periodontitis model. In contrast, the irradiated TBSMSPy$^+$ Gel group exhibited the highest expression level of Runx2, OCN, and ALP among all groups, with values of 15.2, 13.5, and 16.8, respectively. These similar expression levels indicated the cytokines were specifically regulated. It has been demonstrated that NAD$^+$ was a key factor to regulate osteoblast production and bone formation[68–70]. Thus, the similar expression level may be caused by the strong catalytic ability of TBSMSPy$^+$ to oxidize NADH and generate NAD$^+$. However, the

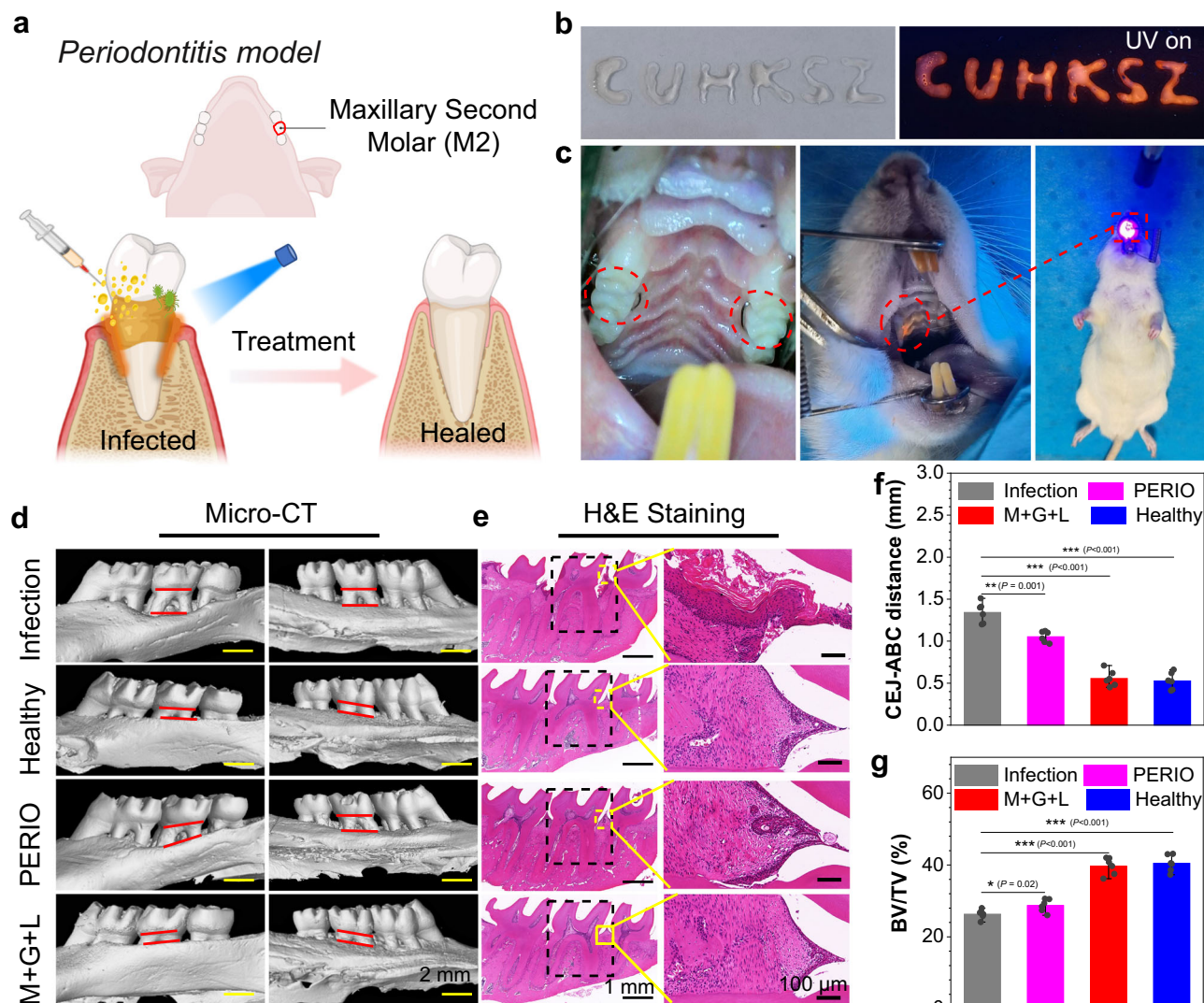**Fig. 6 | Photodynamic periodontitis therapy in vivo. a** Schematic illustration of periodontitis modeling and treatment. Created in BioRender. Zhou, K. (2024) https://BioRender.com/t01g986. **b** Photographs of the injectable TBSMSPy⁺ hydrogel. **c** Photographs of steel suture fixing on the second molar during periodontitis modeling and periodontitis treatment by the injectable TBSMSPy⁺ loaded hydrogels, followed by illumination of a 450 nm laser for 3 min (50 mW•cm⁻²). **d** 3D reconstructions of the maxillary molar area by Micro-CT in different groups ($n = 6$ biologically independent samples, all views show similar results). Red lines mark the distance between CEJ and ABC to reflect the alveolar bone loss. Scale bars 2 mm. PERIO is a medicine for periodontitis treatment, the effective content is minocycline hydrochloride. CEJ: cementoenamel junction, ABC: alveolar bone crest. **e** H&E staining of papillary connective tissue and alveolar bone around the M2 after different treatments, scale bars = 1 mm and 100 μm for low-magnification and high-magnification images, respectively ($n = 6$ biologically independent samples, all views show similar results). **f** Quantitative measurement of CEJ − ABC distance of the M2. **g** The quantitative analysis of bone-related parameters BV/TV from the Micro-CT images. BV: bone volume TV: tissue volume. Data in (**f, g**) are presented as mean ± s.d. derived from $n = 6$ independent biological samples. Statistical significance was assessed via an unpaired two-sided student t-test. NS means not significant, * means $P < 0.5$, ** means $P < 0.01$, and *** means $P < 0.001$.

detailed mechanism remains unclear. We hope this discovery will inspire further research to explore the underlying biological mechanism of photocatalytic systems.

After treatment, a comprehensive assessment of the systemic toxicity of TBSMSPy⁺ Gel was conducted. As shown in Supplementary Fig. 19, H&E staining results of the major organs (heart, liver, spleen, lung, kidney, and stomach) indicated that the implantation of TBSMSPy⁺ Gel with light irradiation did not induce any obvious damage or pathological change. Besides, the body weight of rats had no notable changes (Supplementary Fig. 20). All results presented that TBSMSPy⁺ was friendly to living systems, which indicated the PIRI strategy was suitable for in vivo photocatalytic therapy. Therefore, the abovementioned photocatalytic therapy showed significant promise for potential clinical applications in periodontitis treatment.

Discussion

In summary, a "photoinduced redox imbalance" strategy has been proposed to achieve or enhance oxygen-free photocatalytic therapy. The high TOF (60.7 min⁻¹) of catalyst TBSMSPy⁺ strongly supports this assertion. The multi-step intramolecular electron transfer helps catalyst TBSMSPy⁺ generate more stabilized radical species, interfering with the balance of NADH to NAD⁺, blocking the ATP synthesis pathway, resulting in an energy supply cutoff during DNA replication, leading to bacterial death. In periodontitis photocatalytic therapy, TBSMSPy⁺ demonstrates superior therapeutic effects compared to the commercial medication PIRIO. Moreover, TBSMSPy⁺ displays low toxicity towards normal cells in the absence of irradiation, making it a favorable choice for minimizing treatment-related side effects. The oxygen-free PIRI mechanism holds significant potential for exploring more effective photocatalytic therapy agents.

Methods

Materials
All reactions were performed using standard Schlenk and glovebox (Vigor) techniques under an argon atmosphere. All solvents were distilled before use. All the chemicals used in the experiments were purchased from Energy Chemical Inc., Sigma, Thermo Fisher Scientific Inc., and Sangon Biotech. If no other special was indicated, other reagents and solvents were used as commercially available without further purification. Column chromatographic purification of products was accomplished using 200–300 mesh silica gel.

Ethical statement
All animal experiments were performed following the protocols evaluated and approved by the animal ethical and welfare committee at Xi'an Jiaotong University.

Femtosecond transient absorption (fs-TA) measurements
The fs-TA test was performed using a commercial Helios pump-probe system (Ultrafast System) in conjunction with a regenerative amplified Ti: sapphire laser system (Spectra-Physics, Spitfire Pro). The laser beam, with a pulse duration of 120 fs and wavelength of 800 nm, was divided into two parts: a pump beam and a probe beam. For these experiments, the 400 nm pump beam was employed (the third harmonic of the fundamental was set as 800 nm), and the probe beam was passed through a CaF_2 crystal to generate a 430–760 nm range of continuous white light. All experiments were conducted at 300 K. Data analysis was performed using TAS Analyzer, and graphs were created in Origin 2018. The fitting time traces were complete by robust trust-region reflective Newton nonlinear-least-squares method and fitting to two or three exponentials convolved with a Gaussian-shaped response. Besides, the fitting also included an artifact signal resulting from a cross-phase of the pump and probe. All spectra were chirped in the white light probe and maximum pump-probe temporal overlap was set for time zero. Fs-TA measurements of molecules were carried out to study the photoinduced electron transfer processes.

Photoinduced NADH/NAD⁺ conversion
The photoinduced NADH/NAD$^+$ conversion was assessed by means of UV-vis spectroscopy. Taking TBSMSPy$^+$ as an example, to a 10 × 10 mm quartz cell, 3 mL DMSO containing 3 µM TBSMSPy$^+$ and 180 µM NADH were added. The quartz cell was then exposed to 450 nm laser irradiation (power density:50 mW•cm^{-2}) for different times (0, 20, 30, 40, 50, 60 and 70 s). The corresponding UV-vis spectra were recorded after each irradiation period. If NADH photooxidation occurs, the absorbance of NADH at 339 nm declines. Tests of free NADH, NADH + light, and NADH + TBSMSPy$^+$ were used as controls.

Bacterial NADH detection
The changes in NADH levels in anaerobic cells after the TBSMSPy$^+$-mediated photoredox reaction was confirmed using a NAD$^+$/NADH assay kit obtained from Abcam (ab65348). In brief, *ca.* $1 × 10^6$ bacteria cells per well were cultured in six-well plates at 37 °C in an anaerobic condition, 80% N_2, 10% CO_2, and 10% H_2 atmosphere for 24 h. The cells were then incubated with 3 µM TBSMSPy$^+$ for 24 h, followed by photoirradiation (450 nm, 50 mW•cm^{-2}) for 1 min. For NAD$^+$/NADH extraction, the medium was removed by suction and the cells were harvested by scraping, followed by washing with cold PBS buffer and spinning at 2000 rpm (5 min) so as to obtain cell pellets. The bacterial cells were then extracted using a NAD$^+$/NADH extraction buffer. The samples were filtered using a 10 KD spin column to remove the intracellular enzymes (which could consume NADH rapidly). After heating the collected filtrate at 60 °C for 0.5 h in a water bath, the bacterial NADH content was quantified according to the manufacturer's instructions.

Rats periodontitis model
All animal procedures and experiments about rats in this study were approved by the animal ethical and welfare committee at Xi'an Jiaotong University. All rats were raised and operated in accordance with the guidelines for the care and use of laboratory animals of China and the animal management rules of the Ministry of Health of the People's Republic of China. Three-month-old Wistar male rats were used for periodontitis research.

For modeling of periodontitis, after rats were anesthetized with an intraperitoneal injection of 3% pentobarbital (1 mL kg^{-1}), the maxillary second molar was tied by a 0.25 mm orthodontic steel ligature, and the fixed ligature was kept for 15 days. Meanwhile, the bacterial suspensions, including *P. gingivalis* (10^5 CFUs), and *F. nucleatum* (10^5 CFUs) were instilled around the fixed ligature to create an acute bacterial infection. During this period of 15 days, the rats were given high-sugar drinking water (100 g L^{-1} glucose) to induce periodontitis. After 15 days, the fixed ligature was removed, and the rat periodontitis model was accomplished.

Statistical analysis
All quantitative data in this paper were represented as mean values ± standard deviations. The GraphPad Prism and SPSS software were employed to perform the data processing and statistical analysis. Statistical values of *$P < 0.05$, **$P < 0.01$, ***$P < 0.001$, and ****$P < 0.0001$ were regarded as statistically significant.

Reporting summary
Further information on research design is available in the Nature Portfolio Reporting Summary linked to this article.

Data availability
The data generated in this study are available within the article, Supplementary Information, Source Data, and from corresponding authors upon request. Source data are provided in this paper.

References

1. Yoshida, M., Muneyuki, E. & Hisabori, T. A. T. P. synthase — a marvellous rotary engine of the cell. *Nat. Rev. Mol. Cell Biol.* **2**, 669–677 (2001).
2. Vafai, S. B. & Mootha, V. K. Mitochondrial disorders as windows into an ancient organelle. *Nature* **491**, 374–383 (2012).
3. Titov, D. V. et al. Complementation of mitochondrial electron transport chain by manipulation of the NAD$^+$/NADH ratio. *Science* **352**, 231–235 (2016).
4. Huang, H. et al. Targeted photoredox catalysis in cancer cells. *Nat. Chem.* **11**, 1041–1048 (2019).
5. Dong, S. et al. "Electron transport chain interference" strategy of amplified mild-photothermal therapy and defect-engineered multi-enzymatic activities for synergistic tumor-personalized suppression. *J. Am. Chem. Soc.* **145**, 9488–9507 (2023).
6. Deng, Z. et al. Near-infrared-activated anticancer platinum(IV) complexes directly photooxidize biomolecules in an oxygen-independent manner. *Nat. Chem.* **15**, 930–939 (2023).
7. Xia, S. P. et al. Unexpected photocatalytic degeneration of NAD$^+$ for inducing apoptosis of hypoxia cancer cells. *CCS Chemistry* **5**, 2324–2333 (2022).
8. Shen, Z. et al. Overcoming the oxygen dilemma in photoredox catalysis: Near-Infrared (NIR) light-triggered peroxynitrite generation for antibacterial applications. *Angew. Chem. Int. Ed.* **62**, e202219153 (2023).
9. Chen, Z. et al. Oxygen-tolerant photoredox catalysis triggers nitric oxide release for antibacterial applications. *Angew. Chem., Int. Ed.* **61**, e202204526 (2022).

10. Pham, T. C., Nguyen, V.-N., Choi, Y., Lee, S. & Yoon, J. Recent strategies to develop innovative photosensitizers for enhanced photodynamic therapy. *Chem. Rev.* **121**, 13454–13619 (2021).

11. Gao, Y. W. et al. Multiporphyrinic architectures: advances in structural design for photodynamic therapy. *Aggregate*, e420 (2023).

12. Wang, H. et al. Aggregation-induced emission (AIE), life and health. *ACS Nano* **17**, 14347–14405 (2023).

13. Zhao, P., Li, H. & Bu, W. A forward vision for chemodynamic therapy: issues and opportunities. *Angew. Chem. Int. Ed.* **62**, e202210415 (2023).

14. Juengpanich, S. et al. Pre-activated nanoparticles with persistent luminescence for deep tumor photodynamic therapy in gallbladder cancer. *Nat. Commun.* **14**, 5699 (2023).

15. Tian, J. et al. Activatable Type I photosensitizer with quenched photosensitization pre and post photodynamic therapy. *Angew. Chem. Int. Ed.* **62**, e202307288 (2023).

16. Sun, Q. et al. Cationic telluroviologen derivatives as type-I photosensitizers for tumor photodynamic theranostics. *Aggregate* **4**, e298 (2022).

17. Wang, L. et al. An all-organic semiconductor C(3) N(4) /PDINH heterostructure with advanced antibacterial photocatalytic therapy activity. *Adv. Mater.* **31**, e1901965 (2019).

18. Chen, W. et al. Integration of TADF photosensitizer as "electron pump" and BSA as "electron reservoir" for boosting Type I photodynamic therapy. *J. Am. Chem. Soc.* **145**, 8130–8140 (2023).

19. Lu, Z. & Imlay, J. A. When anaerobes encounter oxygen: mechanisms of oxygen toxicity, tolerance and defence. *Nat. Rev. Microbiol.* **19**, 774–785 (2021).

20. Sevag, M. G. & Ashton, B. Evolution and prevention of drug-resistance. *Nature* **203**, 1323–1326 (1964).

21. Howard, D. H., Scott, R. D. II, Packard, R. & Jones, D. The global impact of drug resistance. *Clin. Infect. Dis.* **36**, S4–S10 (2003).

22. Hu, C. et al. A structural color hydrogel for diagnosis of halitosis and screening of periodontitis. *Mater. Horiz.* **11**, 519–530 (2024).

23. Xu, X. et al. A removable photothermal antibacterial "warm paste" target for cariogenic bacteria. *Chem. Eng. J.* **429**, 132491 (2022).

24. Zhang, M. et al. Photoacoustic imaging-guided self-adaptive hyperthermia supramolecular cascade nano-reactor for diabetic periodontal bone regeneration. *Adv. Sci.* **11**, 2404143 (2024).

25. Goodman, R. P. et al. Hepatic NADH reductive stress underlies common variation in metabolic traits. *Nature* **583**, 122–126 (2020).

26. Liu, X., Zhu, C. & Tang, B. Z. Bringing inherent charges into aggregation-induced emission research. *Acc. Chem. Res.* **55**, 197–208 (2022).

27. Li, M. et al. Photoredox catalysis may be a general mechanism in photodynamic therapy. *Proc. Natl. Acad. Sci. USA* **119**, e2210504119 (2022).

28. Li, M. et al. Conditionally activatable photoredox catalysis in living systems. *J. Am. Chem. Soc.* **144**, 163–173 (2022).

29. Zhang, N., Trépout, S., Chen, H. & Li, M.-H. AIE polymer micelle/vesicle photocatalysts combined with native enzymes for aerobic photobiocatalysis. *J. Am. Chem. Soc.* **145**, 288–299 (2023).

30. Zhang, R. et al. Nickel(II) phototheranostics: a case study in photoactivated H₂O₂-enhanced immunotherapy. *J. Am. Chem. Soc.* **145**, 23257–23274 (2023).

31. Huang, C. et al. In-vitro and in-vivo photocatalytic cancer therapy with biocompatible iridium(III) photocatalysts. *Angew. Chem. Int. Ed.* **60**, 9474–9479 (2021).

32. Sykora, M., Yang, J. C. & Meyer, T. J. Effect of surface immobilization on intramolecular and intermolecular electron transfer in a chromophore–donor–acceptor assembly. *J. Phys. Chem. B* **109**, 1499–1504 (2005).

33. Remacle, F. & Levine, R. D. An electronic time scale in chemistry. *Proc. Natl. Acad. Sci. USA* **103**, 6793–6798 (2006).

34. Teng, K.-X., Niu, L.-Y., Xie, N. & Yang, Q.-Z. Supramolecular photodynamic agents for simultaneous oxidation of NADH and generation of superoxide radical. *Nat. Commun.* **13**, 6179 (2022).

35. Teng, K. X., Niu, L. Y. & Yang, Q. Z. Supramolecular photosensitizer enables oxygen-independent generation of hydroxyl radicals for photodynamic therapy. *J. Am. Chem. Soc.* **145**, 4081–4087 (2023).

36. Shin, Y.-gK., Newton, M. D. & Isied, S. S. Distance dependence of electron transfer across peptides with different secondary structures: the role of peptide energetics and electronic coupling. *J. Am. Chem. Soc.* **125**, 3722–3732 (2003).

37. Heisel, F. & Miehe, J. A. Intermolecular transfer and quenching of electronic excitation-energy in fluid solutions - interpretation of experimental-data with a diffusion-model including distance dependent interaction. *J. Chem. Phys.* **77**, 2558–2569 (1982).

38. Williams, D. F. Assessing the triad of biocompatibility, medical device functionality and biological safety. *Med. Devices Sens.* **4**, e10150 (2020).

39. Adashek, J. J., Goloubev, A., Kato, S. & Kurzrock, R. Missing the target in cancer therapy. *Nat. Cancer* **2**, 369–371 (2021).

40. Wu, X. et al. Reactivity differences enable ROS for selective ablation of bacteria. *Angew. Chem. Int. Ed.* **61**, e202200808 (2022).

41. Tang, Z., Zhao, P., Wang, H., Liu, Y. & Bu, W. Biomedicine meets Fenton chemistry. *Chem. Rev.* **121**, 1981–2019 (2021).

42. Mu, Y. et al. Sensitive and repeatable photoinduced luminescent radicals from a simple organic crystal. *Angew. Chem. Int. Ed.* **60**, 6367–6371 (2021).

43. McCune, J. A., Kuehnel, M. F., Reisner, E. & Scherman, O. A. Stimulus-mediated ultrastable radical formation. *Chem* **6**, 1819–1830 (2020).

44. Li, G. et al. Bacteria-triggered solar hydrogen production via platinum(II)-tethered chalcogenoviologens. *Angew. Chem. Int. Ed.* **61**, e202115298 (2022).

45. Greenfield, S. R., Svec, W. A., Gosztola, D. & Wasielewski, M. R. Multistep photochemical charge separation in rod-like molecules based on aromatic imides and diimides. *J. Am. Chem. Soc.* **118**, 6767–6777 (1996).

46. Rout, Y., Montanari, C., Pasciucco, E., Misra, R. & Carlotti, B. Tuning the fluorescence and the intramolecular charge transfer of phenothiazine dipolar and quadrupolar derivatives by oxygen functionalization. *J. Am. Chem. Soc.* **143**, 9933–9943 (2021).

47. Yu, J. et al. Artificial spherical chromatophore nanomicelles for selective CO₂ reduction in water. *Nat. Catal.* **6**, 464–475 (2023).

48. Veldkamp, B. S. et al. Photoinitiated multi-step charge separation and ultrafast charge transfer induced dissociation in a pyridyl-linked photosensitizer–cobaloxime assembly. *Energy Environ. Sci.* **6**, 1917–1928 (2013).

49. Kim, T., Kim, W., Vakuliuk, O., Gryko, D. T. & Kim, D. Two-step charge separation passing through the partial charge-transfer state in a molecular dyad. *J. Am. Chem. Soc.* **142**, 1564–1573 (2020).

50. Harriman, A., Odobel, F. & Sauvage, J.-P. Multistep electron transfer between porphyrin modules assembled around a ruthenium center. *J. Am. Chem. Soc.* **117**, 9461–9472 (1995).

51. Patgiri, A. et al. An engineered enzyme that targets circulating lactate to alleviate intracellular NADH:NAD⁺ imbalance. *Nat. Biotechnol.* **38**, 309–313 (2020).

52. Teng, K. X. et al. Photo-induced disproportionation-mediated photodynamic therapy: simultaneous oxidation of tetrahydrobiopterin and generation of superoxide radicals. *Angew. Chem. Int. Ed.* **63**, e202318783 (2024).

53. Zhang, Z. et al. Aggregation-induced emission biomaterials for anti-pathogen medical applications: detecting, imaging and killing. *Regen. Biomater.* **10**, rbad044 (2023).

54. Ye, Z. et al. AIEgens for microorganism-related visualization and therapy. *Interdiscip. Med.* **1**, e20220011 (2023).

55. Cantó, C., Menzies, Keir, J. & Auwerx, J. NAD+ metabolism and the control of energy homeostasis: a balancing act between mitochondria and the nucleus. *Cell Metab.* **22**, 31–53 (2015).

56. Scott, J. F., Eisenberg, S., Bertsch, L. L. & Kornberg, A. A mechanism of duplex DNA replication revealed by enzymatic studies of phage phi X174: catalytic strand separation in advance of replication. *Proc. Natl. Acad. Sci. USA* **74**, 193–197 (1977).

57. Kolodner, R. & Richardson, C. C. Replication of duplex DNA by bacteriophage T7 DNA polymerase and gene 4 protein is accompanied by hydrolysis of nucleoside 5'-triphosphates. *Proc. Natl. Acad. Sci. USA* **74**, 1525–1529 (1977).

58. Gellert, M., Mizuuchi, K., O'Dea, M. H. & Nash, H. A. DNA gyrase: an enzyme that introduces superhelical turns into DNA. *Proc. Natl. Acad. Sci. USA* **73**, 3872–3876 (1976).

59. Majumdar, C. & Frankel, F. R. Biological sciences: role of ATP in DNA replication. *Nature* **243**, 33–36 (1973).

60. Bell, S. P. & Stillman, B. ATP-dependent recognition of eukaryotic origins of DNA replication by a multiprotein complex. *Nature* **357**, 128–134 (1992).

61. Tanaka, M., Ohkubo, K. & Fukuzumi, S. Reductive DNA cleavage induced by UVA photoirradiation of NADH without oxygen. *J. Am. Chem. Soc.* **128**, 12372–12373 (2006).

62. Yun, S. H. & Kwok, S. J. J. Light in diagnosis, therapy and surgery. *Nat. Biomed. Eng.* **1**, 0008 (2017).

63. Ciancio, S. G., Mather, M. L. & McMullen, J. A. An evaluation of minocycline in patients with periodontal disease. *J. Periodontol.* **51**, 530–534 (1980).

64. Goodson, J. M. et al. Minocycline HCl microspheres reduce red-complex bacteria in periodontal disease therapy. *J. Periodontol.* **78**, 1568–1579 (2007).

65. Abbas, S., Mahendra, J. & Ari, G. Minocycline ointment as a local drug delivery in the treatment of generalized chronic periodontitis - a clinical study. *J. Clin. Diagn. Res.* **10**, Zc15–Zc19 (2016).

66. Li, J. et al. 2D MOF Periodontitis photodynamic ion therapy. *J. Am. Chem. Soc.* **143**, 15427–15439 (2021).

67. Zhao, X. et al. Injectable hydrogels with high drug loading through B–N coordination and ROS-triggered drug release for efficient treatment of chronic periodontitis in diabetic rats. *Biomaterials* **282**, 121387 (2022).

68. Song, J. et al. Nicotinamide mononucleotide promotes osteogenesis and reduces adipogenesis by regulating mesenchymal stromal cells via the SIRT1 pathway in aged bone marrow. *Cell Death Dis.* **10**, 336 (2019).

69. Li, B. et al. Attenuates of NAD+ impair BMSC osteogenesis and fracture repair through OXPHOS. *Stem Cell Res. Ther.* **13**, 77 (2022).

70. Warren, A. et al. The NAD salvage pathway in mesenchymal cells is indispensable for skeletal development in mice. *Nat. Commun.* **14**, 3616 (2023).

Acknowledgements

Author contributions

K.Z., G.H., Z.Z., and B.Z.T. conceived the idea for the study. K.Z. and S.W. prepared the samples. L.D. conducted fs-TA measurements. K.Z., R.D., and S.S. prepared animal experiments. K.Z. analyzed experiment data. L.X. conducted and analyzed the optical spectra. K.Z., L.D., Z. Z., and B. Z. T. wrote the manuscript. K.Z., L.D., L.X., Z.W., G.Z., G.H., Z.Z., and B.Z.T. revised and polished the manuscript.

Competing interests

The authors declare no competing interests.

Additional information

Supplementary information The online version contains supplementary material available at https://doi.org/10.1038/s41467-024-55060-w.

Correspondence and requests for materials should be addressed to Gang He, Zheng Zhao or Ben Zhong Tang.

Peer review information *Nature Communications* thanks Jianshu Li and the other anonymous reviewer(s) for their contribution to the peer review of this work. A peer review file is available.

Reprints and permissions information is available at http://www.nature.com/reprints

Publisher's note Springer Nature remains neutral with regard to jurisdictional claims in published maps and institutional affiliations.